The Astrophysical Journal, 871:202 (13pp), 2019 February 1 https://doi.org/10.3847/1538-4357/aaf6a8

Spacecraft Radio Frequency Fluctuations in the Solar Corona: A *MESSENGER–HELIOS* Composite Study

David B. Wexler[1,7], Joseph V. Hollweg[2], Anatoli I. Efimov[3], Liudmila A. Lukanina[3], Anthea J. Coster[4], Juha Vierinen[5], and Elizabeth A. Jensen[6]
[1] University of Southern Queensland, Centre for Astrophysics, Toowoomba, Australia; dwexler@mit.edu, David.Wexler@usq.edu.au
[2] Department of Physics, University of New Hampshire, Durham, NH, USA
[3] Kotel'nikov Institute of Radio Engineering and Electronics, Russian Academy of Sciences, Moscow, Russia
[4] MIT Haystack Observatory, Westford, MA, USA
[5] Department of Physics and Technology, University of Tromsø, Tromsø, Norway
[6] Planetary Science Institute, Tuscon, AZ, USA
Received 2018 September 8; revised 2018 November 9; accepted 2018 November 28; published 2019 January 31

Abstract

Fluctuations in plasma electron density may play a role in solar coronal energy transport and the dissipation of wave energy. Transcoronal spacecraft radio sounding observations reveal frequency fluctuations (FFs) that encode the electron number density disturbances, allowing an exploration of the coronal compressive wave and advected inhomogeneity models. Primary FF observations from *MESSENGER* 2009 and published FF residuals from *HELIOS* 1975–1976 superior conjunctions were combined to produce a composite view of equatorial region FF near solar minimum over solar offset range 1.4–25$R_\odot$. Methods to estimate the electron number density fluctuation variance from the observed FF were developed. We created a simple stacked, magnetically structured slab model that incorporated both propagating slow density waves and advected spatial density variations to explain the observed FF. Slow density waves accounted for most of the FF at low solar offset, while spatial density inhomogeneities advected at solar wind speed dominated above the sonic point at 6$R_\odot$. Corresponding spatial scales ranged 1–38 Mm, with scales above 10 Mm contributing most to FF variance. Magnetic structuring of the model introduced radial elongation anistropy at lower solar offsets, but geometric conditions for isotropy were achieved as the slab correlation scales increased further out in the corona. The model produced agreement with the FF observations up to 12$R_\odot$. FF analysis provides information on electron density fluctuations in the solar corona, and should take into account the background compressive slow waves and solar wind-related advection of quasi-static spatial density variations.

Key words: Sun: corona – Sun: oscillations – solar wind – turbulence – waves

1. Introduction

Coronal-heating and acceleration mechanisms remain a challenging research focus in solar physics. Models for energy transfer must account for both the propagation and dissipation of energy from the photospheric sources to the coronal expanse. Intense heating of solar plasma occurs in the transition region and the base of corona, while the plasma acceleration occurs at higher levels of the solar atmosphere, and out into the extended corona. Alfvén wave propagation, which is initiated by transverse motions of the emanating photospheric magnetic field, remains a favored mechanism for transfer of energy into the extended corona. Alfvén waves have been observed in the chromosphere (De Pontieu et al. 2007), transition region and base of corona (Tomczyk et al. 2007; McIntosh et al. 2011). The corresponding Faraday rotation fluctuations observed in radio sounding studies at various coronal heights (Hollweg et al. 1982; Andreev et al. 1997; Jensen et al. 2013; Efimov et al. 2015a, 2015b; Wexler et al. 2017) support the notion of Alfvén waves continuing this energy transport out into the corona and interplanetary space.

The search for mechanisms to explain transfer and dissipation of the Alfvén wave energy in the corona garners continued interest. Dissipation of propagating waves and associated turbulence (Cranmer et al. 2015) constitute one important class of coronal-heating models. Nanoflare-reconnection mechanisms also warrant consideration (Klimchuk 2015; Sakurai 2017) in the investigation of coronal magnetic energy release. Cranmer et al. (2007) and Cranmer (2010) studied 1D simulations of MHD wave dissipation. They modeled an Alfvén wave-based turbulent heating rate for which the exact kinetic mechanism for energy dissipation was not specified. Suzuki & Inutsuka (2005) studied coronal energy dissipation in a 1D MHD simulation using nonlinear Alfvén wave generation of compressive waves and shocks. They found that the energy flux from the slow waves increased with heliocentric radial distance (hereafter solar offset, SO) in the corona, while that of the Alfvén waves decreased. They concluded that slow longitudinal compressive waves may be generated in the corona as part of the energy transfer and dissipation process.

When directed along magnetic field lines in low-beta solar plasma,[8] longitudinal compressive waves may be considered to be acoustic or slow magnetoacoustic (magnetosonic) waves. In this paper, we will apply the terms slow waves, acoustic waves and compressive waves with same intent. Compressive waves have been directly observed as intensity fluctuations propagating from the photosphere to the chromosphere, and observed in the lower corona (Nakariakov & Verwichte 2005). However, unlike the Alfvén waves, the slow waves do not propagate far into the corona. Damping of these waves indicates dissipation,

[7] Guest research student, MIT Haystack Observatory Westford, MA, USA.

[8] Plasma β is the ratio of thermal pressure to magnetic energy density, $\beta = \frac{nk_BT}{B^2/2\mu_0}$.

which suggests their potential importance in coronal energy transfer.

Observational studies of density fluctuations beyond the base of the corona relies on radio sounding techniques. Transcoronal spacecraft radio transmissions will exhibit center frequency fluctuations (FFs) at the receiving radio telescope, caused by refractive index variations in the coronal plasma associated with electron density disturbances. The presence of coronal FF is well-established and may present spectral characteristics that are consistent with turbulence regimes in varying degrees of energy cascade development (Efimov et al. 2010; Yakovlev & Pisanko 2018). Coronal FF signify underlying plasma electron concentration inhomogeneities that may include quasi-static bulk turbulence features convected with the solar wind, as well as compressive waves propagating within the wind (Efimov et al. 1993). In this paper, we speculate that slow compressive waves could be ubiquitous in the corona and contributory to the observed FF power spectra particularly below the sonic point, where the solar wind speed is less than the speed of sound. Fast MHD waves could also produce FF, but may be evanescent in the corona (Hollweg 1978). It has been proposed that coronal magnetoacoustic waves are generated locally via nonlinear interactions of Alfvén waves (Chashei et al. 2005; Efimov et al. 2012).

Quasiperiodic component (QPC) FF spectral enhancements appear intermittently in coronal radio sounding observations (Efimov et al. 2012). Miyamoto et al. (2014) reported on the radial distribution of slow compressive waves in the solar corona using Akatsuki spacecraft radio occultation observations. They identified peaks in FF wavelet analysis and quantified spectral power of the presumed quasiperiodic density waves. They used these isolated QPC wavetrains to estimate the fractional electron density fluctuation based on the idea that the observed FF enhancements were produced wholly by QPC density fluctuations. Their results supported the presence of coronal compressive waves with amplitudes sufficient for nonlinear effects to appear in the region where solar wind initial acceleration occurs. However, estimates of wave energy flux were 1–2 magnitudes less than values obtained from the numerical model of Suzuki & Inutsuka (2005).

In the present study we evaluate FF using combined data from the *MESSENGER* 2009 and *HELIOS* 1975–76 coronal radio sounding observations near superior conjunction. These data give a composite picture of FF for the near-equatorial regions close to solar activity minimum, providing information for SO 1.4–25$R_\odot$. Therefore, we explore the coronal regions of slow solar wind formation and initial acceleration. We present an approach to deduce the density fluctuation spectrum from the power spectrum of observed FF, considering the system as an ensemble of stacked magnetic flux tubes containing uncorrelated density disturbances. Our model shows that compressive waves might contribute significantly to the observed FF at low solar offset, while advected quasi-static spatial density variations impress the signature of solar wind acceleration into the FF observations at solar offset beyond the first few solar radii. In Section 2, we present the observational data and methods to process FF. In Section 3, we present the pertinent radio propagation theory and the method to determine density fluctuation variance, and the related fractional fluctuation parameter. Section 4 develops a two-component model of the frequency measure fluctuation, and then provides the parameters used to implement the model and gives results. In Section 5, a comparison is made between the solar wind speeds based on mass conservation in the flux tube and speed predictions from an established isotropic turbulence bulk flow model (Armand et al. 1987; Efimov et al. 2008), highlighting differences in the lower coronal region for which quasi-static isotropic turbulence models may be inapplicable. Our conclusions are summarized in Section 6.

2. Observations and Data Reduction

Our composite data set consists of primary radio telescope observations of the *MESSENGER* spacecraft in superior conjunction near the solar minimum in 2009, and archival results from *HELIOS* 1 and 2 over 1975–6, again with solar activity near a minimum. Figure 1 illustrates coronal conditions with magnetic field line models (Community Coordinated Modeling Center, CCMC) and source surface synoptic magnetic maps (Wilcox Solar Observatory) for representative Carrington rotations 2090 (*MESSENGER*) and 1642 (*HELIOS* 2). In both cases, the Sun was in a fairly quiet dipole configuration, with equatorial region closed lines that are consistent with overlying streamers.

The *MESSENGER* spacecraft radio data (*X*-band, 8.4 GHz) were recorded with the 100 m Green Bank Telescope with dual polarization feeds to allow determination of the polarization position angles needed to analyze the Faraday rotation. The technical details can be found in Wexler et al. (2017) and Jensen et al. (2013). Here, we explore only the fluctuations in signal frequency. The observations were recorded during ingress to superior conjunction on 2009 November 8, yielding 5000 s of usable data over SO range 1.38–1.49$R_\odot$. Egress recordings were made on 2009 November 10, resulting in 14,400 s of data covering SO range 1.63–1.89$R_\odot$. Figure 2 shows the approximate positioning of the points of closest approach (proximate points) on the sounding line of sight (LOS) during the *MESSENGER* observations, shown on background coronal images for 2009 November 10.

The *MESSENGER* FF data were analyzed in a one-second cadence from primary baseband data, which were recorded at a 5 MHz sampling rate. For each one-second data frame, the radio peak baseband frequency was determined by a Gaussian curve best-fit algorithm applied to the power spectrum of the radio signal. A sample 2000 s record of *MESSENGER* zero-centered radio frequency data is shown in Figure 3(a). Clear fluctuations are evident in the frequency time series (upper panel), along with a slow trend attributed to Doppler shift from the spacecraft motion relative to Earth. For such short data segments, the slow trend was removed with a second-order polynomial fit (Song & Russell 1999). The detrended data constitute the FF time series (lower panel). In the literature, this type data is variably referred to as Doppler residuals, Doppler noise or just (frequency) residuals.

The power spectrum for the sample FF segment is shown in Figure 3(b). Above ~30 mHz, the power-law curve drops into a flat spectral floor. The low-frequency power is reduced by the detrend procedure, which reveals the spectrum that is believed to more accurately reflect the underlying plasma density fluctuations. The sample spectrum shows enhanced spectral density over 5–7 mHz, consistent with a QPC. The variance of FF, $\sigma^2_{\rm FF}$, was obtained from numerical integration over a specified frequency band (see next section). The lower limit was set by the record length and the upper limit was set to a

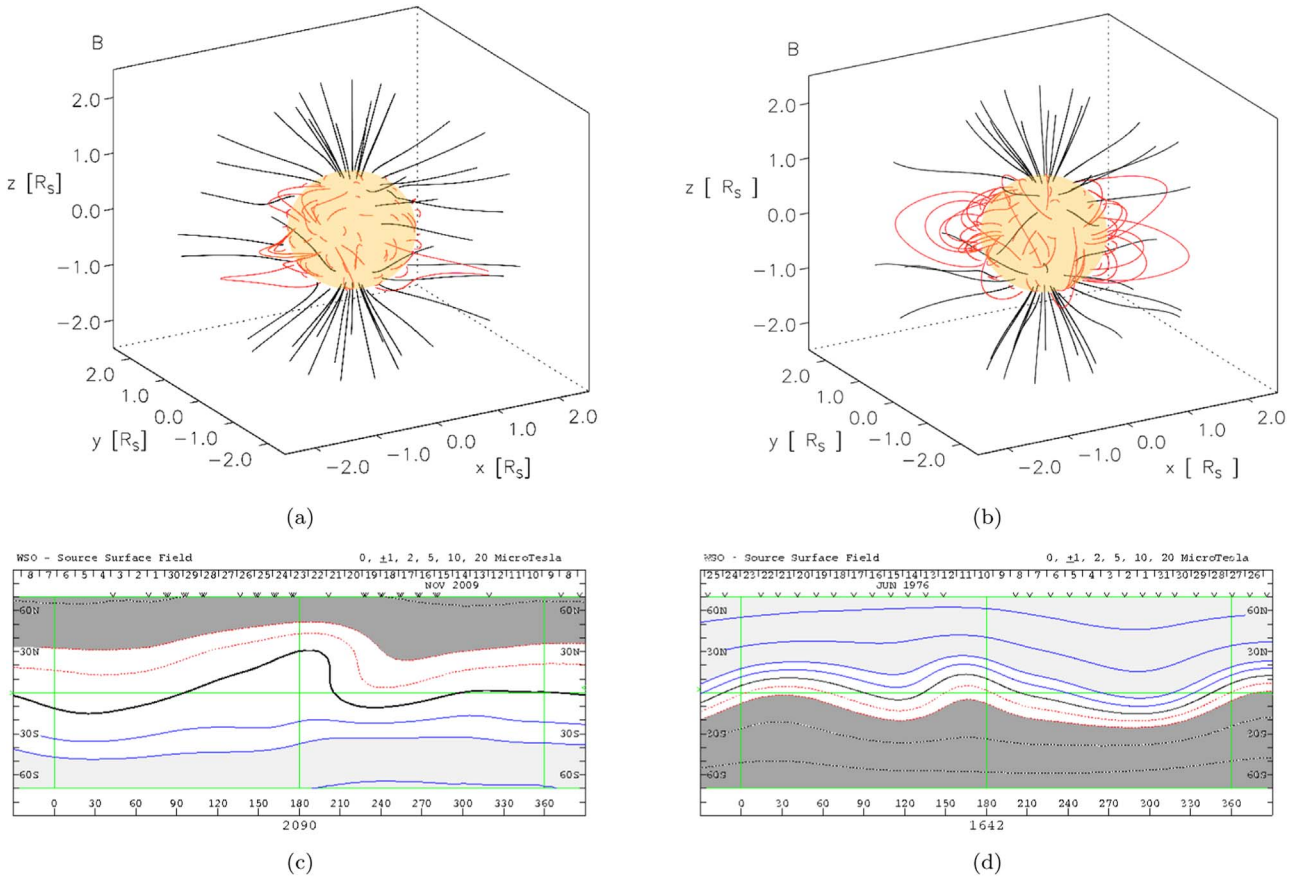

Figure 1. Magnetic field modeling from solar surface to $2.5R_{\odot}$ from the Community Coordinated Modeling Center. (a) CR 2090, *MESSENGER* egress data 2009, (b) CR 1642, corresponding to part of the *HELIOS* 2 data 1976. Potential field source surface magnetic maps ($2.5R_{\odot}$) for the Wilcox Solar Observatory: (c) *MESSENGER* CR 2090 (d) *HELIOS* CR 1642.

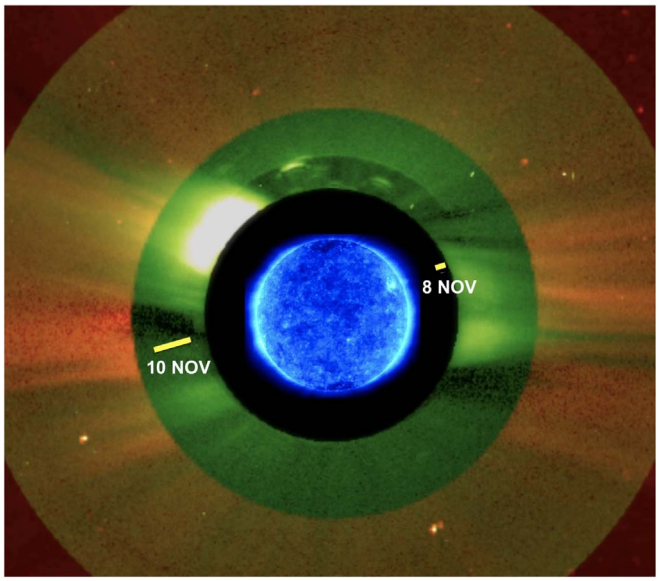

Figure 2. Approximate positioning of the LOS proximate points during the *MESSENGER* observations, shown on background images of *STEREO B* COR1 (green hues starting at inner occluding disk rim) and *SOHO* LASCO C2 (orange hues) for 2009 November 10. The COR1 streamer configuration is only approximate because *STEREO B* was aligned obliquely to the *MESSENGER* LOS toward Earth. The central inset is an EIT 171 Å image from *SOHO* for the same date.

frequency below which the power spectrum drops into the noise floor (the theoretical upper limit may be as high as the Nyquist frequency: 0.5 × sampling rate in s^{-1}). Our practical range for frequency integration to obtain σ^2_{FF} was 1–28 mHz.

In the *MESSENGER* data, considerable variability was noted in the spectral index. Sporadic presentation of localized enhanced spectral power was noted. Individual data segments showed spectral indices below or above the classic Kolmogorov 2/3 spectral index[9] for FF. The spectral index determination is sensitive to the detrend method, frequency range for index line fit, noise reduction, and smoothing, and therefore should be interpreted cautiously in the present limited data set. The spectral index was fitted over 1–10 mHz. Our method for power spectral processing included extraction of the mean high-frequency noise floor and application of a 5-point smoothing algorithm with 1:2:3:2:1 weighting. For the *MESSENGER* data, we found the average spectral index in ingress to be $\alpha = 0.55 \pm 0.08$ and in egress, $\alpha = 0.58 \pm 0.10$.

The *HELIOS* FF data (*S*-band, 2.3 GHz) were obtained from JPL's Deep Space Network Progress Reports (Berman & Rockwell 1975; Berman et al. 1976), already in integrated form. These reports provided the best (i.e., smallest) noise estimates by averaging three selected groups of 10–20 averaged values judged to provide the lowest noise values (as rms) for a

[9] Spectral index, α, is presented using positive index convention; the actual log-log spectral slope is negative.

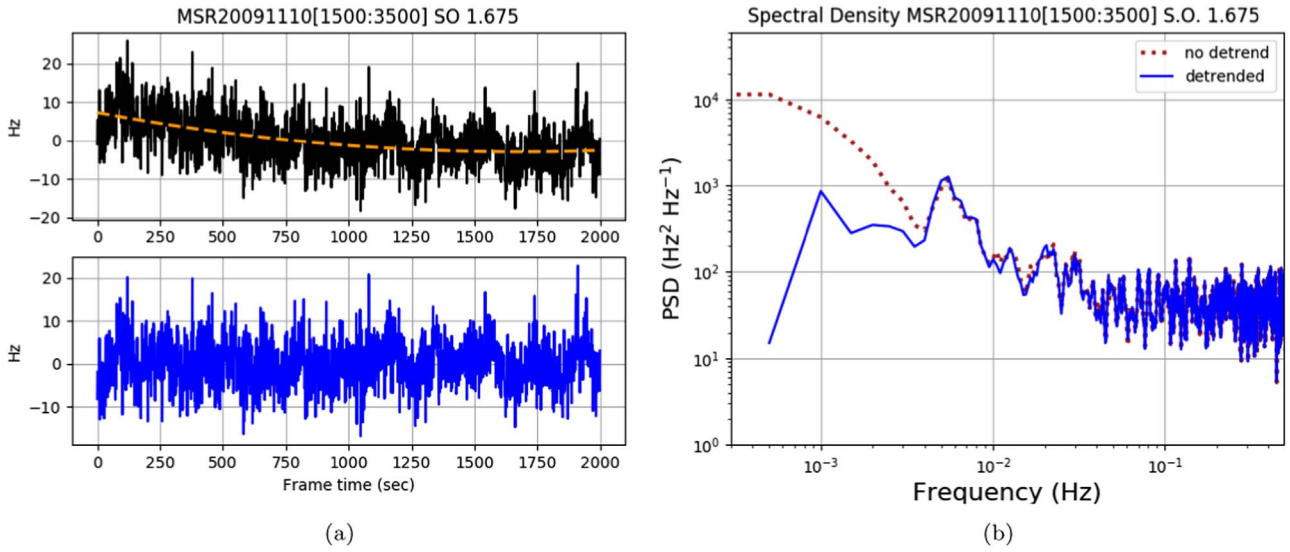

Figure 3. Left-hand panel: time series of zero-centered frequency data. The upper panel shows the FF time series for a 2000 s analysis frame, at SO 1.675 $R_\odot$. The dashed line is the second-order polynomial used to remove the slow trend attributed to the Doppler shift of spacecraft motion. The lower panel shows the FF time series after the detrend procedure was applied. Right-hand panel: power spectral density (PSD) of the FF analysis segment. The detrend procedure mostly affects low-frequency spectral power, as shown with the dotted line. In this sample, enhancement of spectral power over 5–7 mHz relative to the background spectrum is noted.

60 s data sampling rate. The frequency data were obtained from various DSN ground tracking stations: 11, 12 and 14 in California, US, 42 and 43 in Canberra, AU and 61 and 62 in Madrid, Spain. The *HELIOS* data were reported in two cycles of observations for superior conjunction in 1975, covering DOY 96–166, and DOY 227–251, and one cycle of observations from *HELIOS* 2 in 1976, DOY 120–165. The *HELIOS* data covered heliocentric offset range 2.22–25$R_\odot$.

The FFs are sensitive to radio transmission wavelength λ (see Section 3). We combined the *MESSENGER* and *HELIOS* data sets by using the radio wavelength-independent rms FF measure $\sigma_{\rm FM}$, which is defined as

$$\sigma_{\rm FM} = \frac{\sqrt{\sigma_{\rm FF}^2}}{\lambda}. \quad (1)$$

For the *S*-band observations, $\lambda = 0.1304$ m and for *X*-band, $\lambda = 0.0357$ m. The frequency-fluctuation measure (FM) is analogous to the rotation measure used for Faraday rotation. A summary of the *MESSENGER–HELIOS* primary $\sigma_{\rm FM}$ composite data is given in Figure 4.

To make the *HELIOS* frequency measure fluctuation observations comparable to those from *MESSENGER*, two factors needed consideration. The first was correction for the *HELIOS* two-way signal exposure to plasma inhomogeneities. In general, addition of variances for time series x and y may combined as $\sigma_{x+y}^2 = \sigma_x^2 + \sigma_y^2 + 2\text{covariance}(xy)$. In completely uncorrelated x and y fluctuations, the covariance is zero, so the addition of x and y variances is simply the sum of individual variances. However, in the case of completely correlated x and y signals, say $x = y$, the covariance$(xy) = \sigma_x^2$ and the total variance for the doubled path becomes $4\sigma_x^2$.

Two-way transmission enhancement in *HELIOS* sounding data was described by Efimov et al. (2004). In a two-way regime, an outgoing terrestrial radio transmission crosses the corona en route to the spacecraft. The spacecraft then returns a phase-linked signal back through the corona to the receiving system on Earth. Spacecraft transmissions sent from the outer heliosphere should have fluctuations uncorrelated to those of

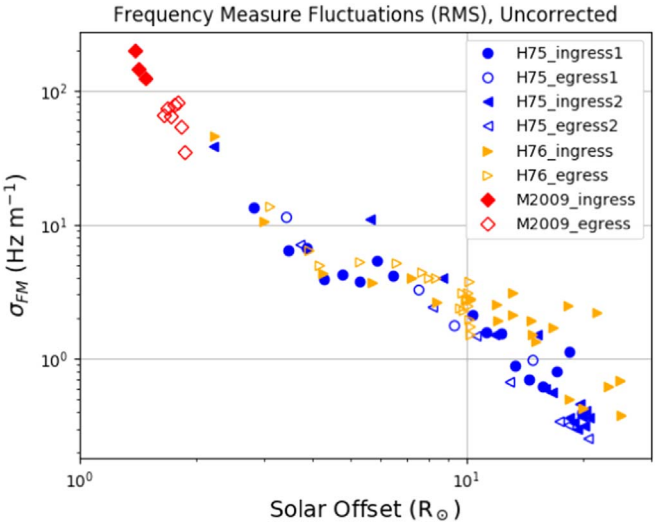

Figure 4. Composite of the frequency measure fluctuations, $\sigma_{\rm FM}$. The *MESSENGER* data were obtained in a one-way radio configuration. The 2-way *HELIOS* data shown here were taken directly from JPL technical reports, normalized to radio wavelength, but not yet corrected for correlated 2-way propagation inhomogeneities and the difference in effective frequency band.

the original inbound signal because the coronal plasma density inhomogeneities should have moved and changed during the interval required to reach the spacecraft and back. For these uncorrelated fluctuations, $\sigma_{\rm FM}^2$ arising from a two-way path would be twice that of a one-way observation. However, the inner heliospheric positioning of *HELIOS* during the 1975–6 sounding campaign resulted in largely correlated fluctuations on the return path, bringing the total variance to four times that of a one-way trip.

An additional correction was required to compensate for the difference in effective integration bands between *HELIOS* and *MESSENGER* data. *HELIOS* observations, with one-minute frequency residual sampling over an average of 15 minutes, resulted in a frequency band 1.11–8.33 mHz. Assuming a spectrum of the Kolmogorov form, the variance obtained from

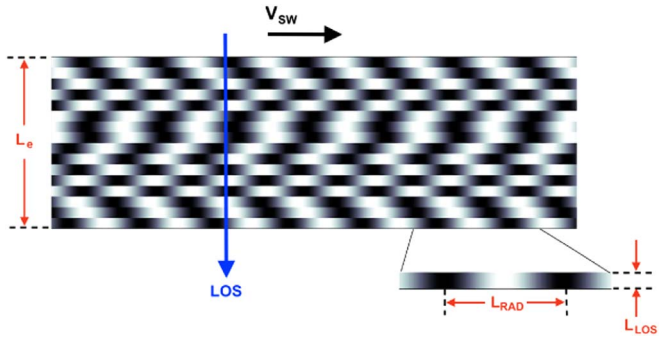

Figure 5. The simplified scheme of oscillating density fluctuations aligned parallel to the magnetic field, in a series of stacked slabs. Each horizontal strip contains plasma density oscillations, illustrated by brightness variations. $L_{\rm RAD}$ is the horizontal length scale for convected quasi-static density disturbances. The vertical scale $L_{\rm LOS}$ corresponds to magnetically determined correlation length. The bulk plasma frame outflow speed is $V_{\rm SW}$. Density fluctuations combine with random-walk statistics to yield the rms fluctuation for the effective LOS, L_e.

the 1.11–8.33 mHz band was about half the variance obtained over 1–28 mHz, to within 5%. Combining the two separate effects on *HELIOS* variance, the Doppler residuals were multiplied by two for the bandwidth correction but divided by four to correct for the correlated two-way propagation. Taken together, the net correction was a division of the reported *HELIOS* variances by two (rms by $\sqrt{2}$), to approximate equivalence with the one-way *MESSENGER* variance.

3. The FFs Model

Radio propagation theory indicates that variations in the signal frequency observed at the radio telescope, f_{obs}, are related to the original transmitted frequency, f_0, by fractional Doppler shift due to spacecraft velocity $V_{\rm rel}$ relative to the radio LOS, and the time rate of change in electron density across the LOS (Efimov et al. 2007; Pätzold et al. 2012; Jensen et al. 2016); also see Hollweg & Harrington (1968), Vierinen et al. (2014):

$$f_{\rm obs} = f_0 - \frac{V_{\rm rel}}{c} f_0 + \frac{1}{2\pi} r_e \lambda \frac{d}{dt} \int_0^L n_e(s, t) dS \qquad (2)$$

where $\lambda = \frac{c}{f_0}$ is the radio transmitter wavelength, c is the speed of light, n_e is the electron number density, dS is the LOS integration path increment and the classical electron radius, $r_e = 2.82 \times 10^{-15}$ m, is

$$r_e = \frac{e^2}{4\pi\epsilon_0 m_e c^2}, \qquad (3)$$

S.I. units are used throughout unless otherwise noted.

Here we develop a simplified coronal model consisting of stacked slabs (Figure 5), which is intended to represent the series of parallel, uncorrelated density fluctuation structures through which the sounding radio signal passes. In each slab, we treat the electron density as varying in time and space along the solar radial axis but vertically constant at a given moment over the integration element length $L_{\rm LOS}$. The slab height (or width) is set to the correlation scale of field line fluctuations based on local magnetic field strength (see Section 4). Thus the slabs are partitioned, by magnetically controlled scaling, into horizontal elements that contain the density fluctuations. Note that the slabs are defined within the continuous coronal magnetic field.

When the Doppler shift is removed by a suitable detrend procedure (assuming that the spacecraft motion is a slowly changing variable that can be well-represented by trajectory data or a mathematical function), then the equation for instantaneous FF of the radio signal frequency, $\delta f(t) = f_{\rm obs}(t) - f_0$, for a single slab simplifies to

$$\delta f(t) = \frac{1}{2\pi} r_e \lambda L_{\rm LOS} \frac{d}{dt} n_e(t). \qquad (4)$$

The electron number density includes a mean electron number density $n_e(r)$ and a fluctuating component of amplitude δn_e. Only the fluctuating component will contribute to the observed FF. For a density oscillation of form $\delta n_e(t) = \delta n_e \exp^{-i\omega t}$, the time derivative has magnitude $\omega \delta n_e$. This relation is captured in the Fourier transform:

$$\mathcal{F}\{\delta f(t)\} = \frac{-i}{2\pi} r_e \omega \lambda L_{\rm LOS} \mathcal{F}\{\delta n_e(t)\}. \qquad (5)$$

Then, using the FF power spectral density for a data segment of temporal length T, notated $|{\rm FF}(\omega)|^2$ and given as $\frac{1}{T}\mathcal{F}\{\delta f(t)\}\mathcal{F}^*\{\delta f(t)\}$, we find

$$|{\rm FF}(\omega)|^2 = \frac{1}{4\pi^2} r_e^2 \lambda^2 \omega^2 L_{\rm LOS}^2 |\delta n_e(\omega)|^2 \qquad (6)$$

where $|\delta n_e(\omega)|^2$ is the corresponding power spectral density of electron concentration fluctuations.

In terms of the oscillation frequency in Hz, $\nu = \omega/2\pi$, and converting to radio-wavelength normalized fluctuation measure FM (Equation (1)), we obtain

$$|{\rm FM}(\nu)|^2 = r_e^2 \nu^2 L_{\rm LOS}^2 |\delta n_e(\nu)|^2. \qquad (7)$$

The electron concentrations along the LOS are generally greatest near the proximate point. The heliocentric distance, R, to the proximate point is the "solar offset" (SO). This radial distance, when given in solar radius units ($R_\odot$), will be notated r; $R = rR_\odot$. For radio sounding studies, the LOS integration path lengths are typically considered SO/2 in either direction from the proximate point for spherically symmetric coronal models, giving an effective integration length L_e equal to R. The randomized density fluctuations of individual elements combine on the LOS as a sum of individual variances. Using Equation (7) for a single slab, multiplication by the number of stacked elements $R/L_{\rm LOS}$ gives the relation between the FM spectrum and the underlying n_e fluctuation spectrum as

$$|{\rm FM}(\nu)|^2 = r_e^2 \nu^2 L_{\rm LOS} R |\delta n_e(\nu)|^2. \qquad (8)$$

Thus knowledge of the FM power spectrum from observations can be readily used to determine the implied electron density fluctuation power spectrum (Figure 6). Note that this expression does not depend on which physical mechanism (e.g., propagating waves versus bulk outflow of density inhomogeneities) produces the density fluctuations on the sounding LOS. There is no assumption about the state of turbulence. We will clarify these contributions in Section 4.

In a pure radial slab configuration, the LOS contributions would increase with azimuthal fan-out angle ϕ as $L_{\rm LOS}/\cos\phi$. For a fan-out from the equator of no more than $\pm 30°$, the maximum increase would be about 15% at the wings and most of the LOS path would have an increase in $L_{\rm LOS}$ of less than 10%. We chose the simplified scheme of stacked horizontal elements to represent the radial slab structures ($\phi = 0$).

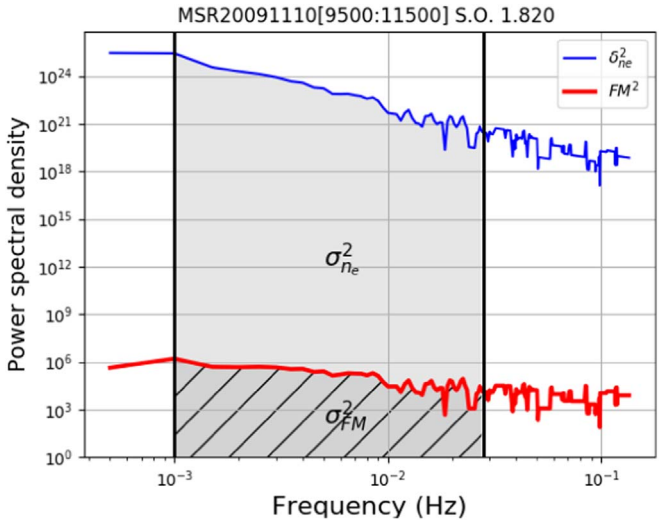

Figure 6. The electron density fluctuation power spectrum δn_e^2 (upper, blue curve) is calculated from the FM power spectrum (lower, thick red curve) FM^2 using Equation (8). The variances $\sigma^2_{\rm FM}$ and $\sigma^2_{n_e}$ are integrated quantities shown as the hatched and light filled areas respectively, in the 0.001–0.028 Hz frequency band.

Integrated measures are used to represent the spectral density information in consolidated form to facilitate comparisons. The *HELIOS* data were only available in the form of variances and were unavailable as primary spectral data. This limitation required Equation (8) to be reworked into a format based on integrated quantities. The goal is to obtain the number density fluctuation information based on knowledge of the FF spectrum or even just the FF variance.

The fluctuation variances $\sigma^2_{\rm FM}$ and $\sigma^2_{n_e}$ are defined for frequency integration range $[a,b]$ by

$$\sigma^2_{\rm FM} \equiv \int_a^b |{\rm FM}(\nu)|^2 d\nu \tag{9}$$

$$\sigma^2_{n_e} \equiv \int_a^b |\delta n_e(\nu)|^2 d\nu. \tag{10}$$

Equations (8) and (10) may be combined to give

$$\sigma^2_{n_e} = \frac{1}{r_e^2 L_{\rm LOS} R} \int_a^b \frac{|{\rm FM}(\nu)|^2}{\nu^2} d\nu. \tag{11}$$

These variances, which are represented as filled areas under the curves in Figure 6, can be obtained by numerical integration when the FM power spectrum is specified. In contrast, the *HELIOS* FF data were given only as variances, so we treated the curves as idealized, single power-law spectra in order to estimate σ_{n_e} as follows.

Assuming that the FM power spectrum follows a power law of the form $|{\rm FM}(\nu)|^2 = \zeta \nu^{-\alpha}$, we may evaluate the integrals in Equations (9) and (11) over frequency range $[a,b]$ as

$$\sigma^2_{\rm FM} = \frac{\zeta}{1-\alpha} \nu^{(1-\alpha)}\Big|_a^b \tag{12}$$

$$\sigma^2_{n_e} = \frac{-1}{(\alpha+1)} \frac{\zeta}{r_e^2 L_{\rm LOS} R} \nu^{-\alpha-1}\Big|_a^b. \tag{13}$$

For a known $\sigma^2_{\rm FM}$ and α, we can estimate ζ observationally, although it cancels out in the subsequent Equation (14). We tested relation (10) with 2000 s *MESSENGER* data segments and found that, when using spectral index fitted over 1–10 mHz on the power spectrum, the estimated variance matched the computationally integrated value for range 0.001–0.028 Hz within 10%.

Equation (8) can be placed in the form of variances for FM and δn_e by integrating both sides using expressions (9)–(11), then substituting in relations (12) and (13) to obtain

$$\sigma^2_{\rm FM} = r_e^2 \nu_c^2 L_{\rm LOS} R \sigma^2_{n_e} \tag{14}$$

provided a scaling frequency ν_c is found from:

$$\nu_c^2 = \frac{\alpha+1}{\alpha-1} \frac{\nu^{1-\alpha}\big|_a^b}{\nu^{-\alpha-1}\big|_a^b}. \tag{15}$$

Therefore, $\sigma^2_{n_e}$ can be estimated from known $\sigma^2_{\rm FM}$ if spectral index α is known or well-approximated. This specific electron number density variance is pertinent only for the given frequency range, here 1–28 mHz. Similarly, the scaling frequency ν_c is linked to the specific integration frequency range (the "observation window") and the applicable spectral index for the data under study.

The fractional density fluctuation ϵ is defined as

$$\epsilon = \frac{\sigma_{n_e}}{n_e} \tag{16}$$

where the mean local electron number density $n_e(r)$ may be estimated by a parameter model or calculated from dual-frequency ranging data. Finally, Equations (14) and (16) are consolidated to produce

$$\epsilon = \frac{\sigma_{\rm FM}}{r_e \nu_c n_e \sqrt{L_{\rm LOS} R}}. \tag{17}$$

This is the observational model for ϵ based on randomized density fluctuations on the LOS in a stacked slab coronal plasma. It is important to note that while ϵ is a useful marker of electron density disturbances, the values must be interpreted in the context of the specific integration frequency limits, accuracy of ν_c (knowledge and stability of the spectral index) and suitability of the electron number density model. All of the factors that influence $\sigma_{\rm FM}$, such as of shifting frequencies on the sounding LOS from acceleration of the solar wind, may be impressed into the observational determination of ϵ. In the next section we will implement Equation (17) to present the ϵ derived from the *MESSENGER*/*HELIOS* FF observations then develop a two-component density fluctuation model that incorporates the effect of solar wind outflow.

4. Implementation and Results

A number of coronal electron number density models exist, several of which are reviewed by Bird & Edenhofer (1990). A standard model for electron number density is the Allen–Baumbach formula, which was derived from coronagraph eclipse observations of the K-corona:

$$n_e(r) = \left(\frac{2.99}{r^{16}} + \frac{1.55}{r^6}\right) \times 10^{14} \tag{18}$$

in $\rm m^{-3}$. The first term on the right is important at close SO, $<\approx 1.2 R_\odot$, while the second term was intended to be applicable out to 2–3 Rs. The model assumes spherical symmetry. To extend the range of number density estimates into the extended corona, a third term with a near inverse square power

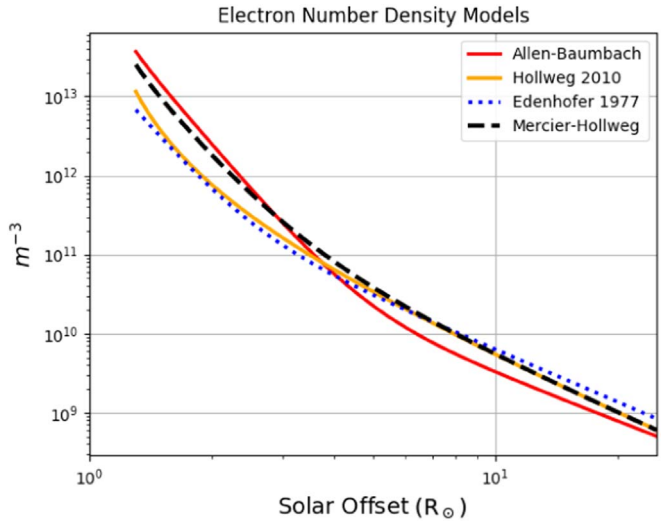

Figure 7. Electron number density models. Our composite model, combining the fit from Mercier & Chambe (2014) with the second term from Hollweg et al. (2010), is shown with a dashed line. For comparison purposes, the Allen–Baumbach, Hollweg and Edenhofer models are given.

relationship is usually added. The deviation from an exact 2 exponent in the added term is attributed to acceleration of the solar wind (Pätzold et al. 1997). Advanced models may also specify the heliolatitiude.

Number densities may be an order of magnitude higher in streamer regions than in the fast solar winds above coronal holes. This is of considerable significance to our study of the equatorial regions near solar minimum, when the streamers are usually organized broadly about the equatorial zones. Patzold et al. (1987) review electron number density models pertinent to the 1975–1976 *HELIOS* data that we used in this study. They present the results from Edenhofer et al. (1977), which give the formula for number density in the 1976 *HELIOS* data based on ranging time-delays of the spacecraft radio signals:

$$n_e(r) = \left(\frac{30}{r^6} + \frac{1}{r^{2.2}}\right) \times 10^{12}. \tag{19}$$

Their formula was intended to represent the number densities over $3 < R < 65R_\odot$. Hollweg et al. (2010), while fitting results from Cranmer et al. (2007), provided a number density model for a streamer along heliolatitude 28° over $2 < R < 30R_\odot$:

$$n_e(r) = 7.68 \times 10^{11}(r-1)^{-2.25}. \tag{20}$$

We reasoned that Equation (20) was well-suited for our *HELIOS* data but that an additional term applicable to the low solar offset *MESSENGER* data would be needed. For this purpose, we used the average of 2008 and 2010 equatorial electron number density determinations from Mercier & Chambe (2015) fitted over $1.2–1.5R_\odot$. The resulting hybrid formula (hereafter, Mercier–Hollweg formula) that was used in the present study is:

$$n_e(r) = \left(\frac{65}{r^{5.94}} + \frac{0.768}{(r-1)^{2.25}}\right) \times 10^{12}. \tag{21}$$

In Figure 7, we show a comparison of these electron number density models. The hybrid model used for our analysis is shown as a dashed line.

LOS element integration length $L_{\rm LOS}$ (sometimes referred to as the correlation scale), in our model is considered equivalent to the magnetic autocorrelation scale, which is related to spacing between photospheric magnetic flux tubes where the field line perturbations originate. This width has been related to the inverse square root of background magnetic field strength (Spruit 1981; Hollweg et al. 1982). We set the LOS element integration length according to Hollweg et al. (2010), as used in their analysis of *HELIOS* Faraday rotation fluctuations:

$$L_{\rm LOS} = 3.35 \times 10^6 r^{0.918} \tag{22}$$

in meters.

The results for Equation (17), ϵ as a function of solar offset, are shown in Figure 8(a). Individual data points were calculated using the observational input $\sigma_{\rm FM}$, spectral index $\alpha = 0.5$ and frequency integration limits 0.001–0.028 Hz; $\nu_c = 0.0036$ Hz. If we accept the number density model Equation (21) as being accurate for this data set, then the uncertainty in ϵ is dominated by the variation in ν_c, and thus by choice of spectral index. For the *HELIOS* data, the spectral index had to be guessed—we chose $\alpha = 0.5$ but considered this accurate only within a factor of two. By using a factor of two change in α for the *MESSENGER* data of known spectral index and directly computed ϵ, we found that the uncertainty in ϵ was 30%. The vertical error bars in Figure 8(a) show the effect of this factor of two uncertainty in α. This figure also shows the results using the two-component ϵ model that is developed next (Equation (34)), applied with $\alpha = 0.3$, 0.5, 0.67 and uncertainty bands shown for the $\alpha = 0.5$ model results.

The baseline level for fractional density fluctuation found over S.O. $\sim$1.4–1.7 $R_\odot$ is about 0.017. There is modest increase in ϵ up until $5R_\odot$, and then there is a sharper rise in values over $5–7R_\odot$. This pattern of increasing fractional electron density fluctuation with increasing solar offset has been reported previously, e.g., (Hollweg et al. 2010; Miyamoto et al. 2014). However, the reasons why ϵ increases with increasing solar offset remain speculative. Miyamoto et al. (2014), following Suzuki & Inutsuka (2005), suggested that the ϵ increases found in quasiperiodic wave spectral enhancements were due to locally generated slow density waves related to nonlinear Alfvén wave interactions, and thus a stage of energy transfer within the corona. Others, like Hollweg et al. (2010) present the result more phenomenologically, building the case that the fractional density fluctuations, whatever their source, were too small to account for the observed coronal Faraday rotation fluctuations.

It is useful to compare the plot of ϵ in Figure 8(a) with estimated solar wind speed, $V_{\rm SW}$, and the speed of sound, C_s, in Figure 8(b). The speed of sound is found from

$$C_s = \sqrt{\frac{\gamma k_B T}{m_p}} \tag{23}$$

with ratio of specific heats $\gamma = 5/3$, proton mass m_p, Boltzmann constant k_B and coronal temperature T in Kelvins. Coronal temperature was estimated by a fit to data presented by Newkirk (1967), in which it was considered $T_i = T_e = T$ based on the available information. Specifically the coronal temperature was estimated as

$$\log T = -0.54 \log(r) + 6.30 \tag{24}$$

such that the temperature dropped from 2.2×10^6 K at the solar surface to 0.4×10^6 K at SO $= 20R_\odot$.

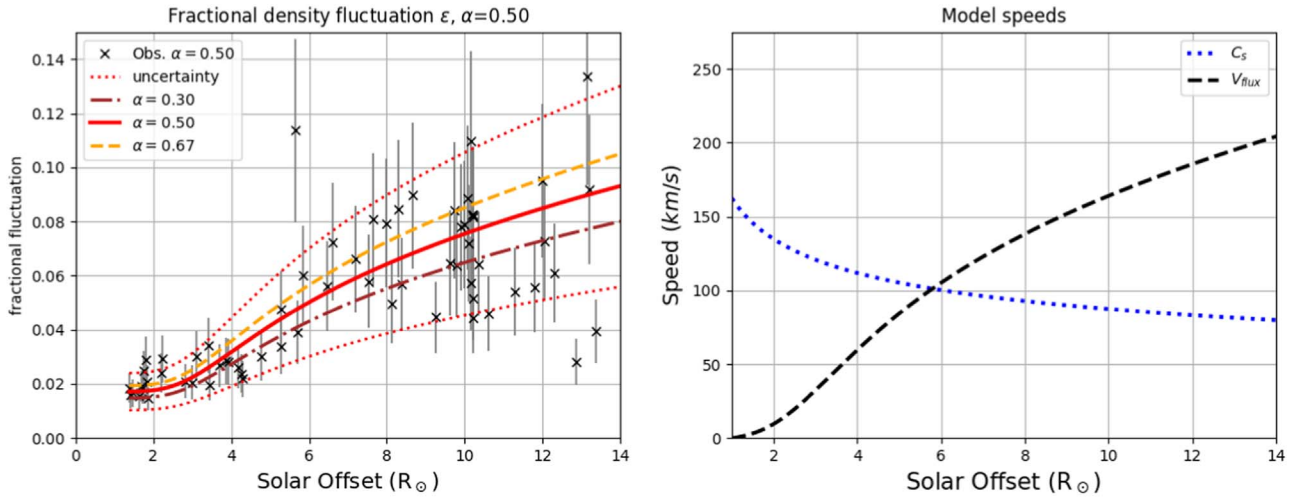

Figure 8. (a) Fractional electron density fluctuation ϵ (crosses), as calculated (Equation (17)) for the specified integration frequency band and with $\alpha = 0.5$; the wide error bars are due mostly to factor of two uncertainty in α. The solid line shows the model for ϵ developed from combined acoustic wave and convected density variances (Equation (35)). The model itself has only modest sensitivity to choice of α but the error bars are wide, primarily due to uncertainty in ν_c which is highly sensitive to α. (b) Modeled mass flux speed $V_{\rm flux}$ and sound speed C_s. The plasma speeds for mass conservation in the flux tubes were used to represent solar wind speed $V_{\rm SW}$ in implementation of the FF model.

The solar wind outflow speed, $V_{\rm SW}$, is modeled on mass conservation in the horizontal slab elements:

$$n_e L_{\rm LOS}^2 V_{\rm flux} = \text{constant}. \quad (25)$$

To enact the wind speed model, we specify $V_{\rm flux} = 250\ {\rm km\ s^{-1}}$ at $r = 20R_\odot$. This is a reasonable value for slow solar wind speed at that solar offset, in accordance with studies in optical (Sheeley et al. 1997), radio intensity scintillation (Imamura et al. 2014) and dual-frequency radio analysis (Muhleman & Anderson 1981). The modeled solar wind speeds and sound speeds are shown in Figure 8(b). The sonic point is at $\sim 6R_\odot$, which is consistent with the 5–$7R_\odot$ range mentioned by Efimov et al. (1993), and intermediate between lows of $2.5R_\odot$ (Suzuki & Inutsuka 2005) to $3.5R_\odot$ in wave-heating simulations (Cranmer et al. 2007) and an upper range 12–14 $R_\odot$ discussed by Yakovlev & Pisanko (2018).

It is interesting that the inflection in ϵ, at $r = 6R_\odot$, occurs in the region of the estimated sonic point. This observation suggests the possibility that the observed FF may be dominated by the "frozen-in", and slowly changing, advected density inhomogenieties near and above the sonic point. Propagating slow compressive waves (acoustic or slow magnetoacoustic) could then provide the main contribution below the sonic point.

We now explore the basis for the observed increase in ϵ with increasing solar offset. The key observational input is $\sigma_{\rm FM}$. In our method, the "observational window" is a fixed bandwidth [a,b] that is built into the scaling frequency ν_c, such that an observed increase in $\sigma_{\rm FM}$ must be associated with a corresponding increase σ_{n_e} for a given SO (see Equation (14)). We investigate whether the advection of density disturbances across the sounding LOS by solar wind bulk outflow can explain the radial dependence of observational ϵ that was demonstrated in Figure 8(a).

A two-component model for ϵ and $\sigma_{\rm FM}^2$ is proposed, based on two premises: (1) the quiet, equatorial corona must have some basal spectrum of density inhomogeneities from propagating slow density waves and quasi-static spatial density variations, and (2) the density oscillations advected with the solar wind flow present frequency-shifted spectral information to the sounding LOS observational window. Given the negative power law form of the density and FM fluctuation spectra, a right-shifted power spectrum will bring increased power into the fixed observational frequency window. It will be shown that the propagating slow density waves will dominate the observational $\sigma_{\rm FM}$ and ϵ at low S.O., while the advected spatial spectrum of density variations will dominate when the solar wind speed prevails over the local speed of sound.

The two-component model that is developed below requires a number of assumptions and the use of established parameter formulae. Specifically, it will require models for radial dependence of the speed of sound, solar wind outflow speed, coronal streamer background electron number density and a choice of characteristic length scale for the quasi-static spatial density variations. We assume that a baseline level of fractional density fluctuation, $\epsilon_{\rm BL}$ is present throughout the coronal region under study when referenced to the comoving solar wind frame and the same frequency band (here, 1–28 mHz). Our starting point is $\epsilon_{\rm BL} = 0.017 \pm 0.002$, as found from results in Figure 8(a), averaged over S.O. 1.4–$1.7R_\odot$, where there is relatively little effect from solar wind. Given that we wish to provide the simplest explanation for the SO-dependence of ϵ with the fewest assumptions, we set $\epsilon_{\rm BL}$ to apply equally as the fractional rms amplitude for both the density waves and the spatial inhomogeneities. In addition, it should be noted that the possibility of $\epsilon_{\rm BL}$ changing with time or position is not considered in this model. The model that we propose can be modified to incorporate such refinements when new data that allow discrimination of density sources become available.

In this model, we predict that the increase in observed ϵ (Equation (17)) relative to $\epsilon_{\rm BL}$ will be the ratio of a shifted scaling frequency $\nu_{\rm shift}$, which includes the effect of advection

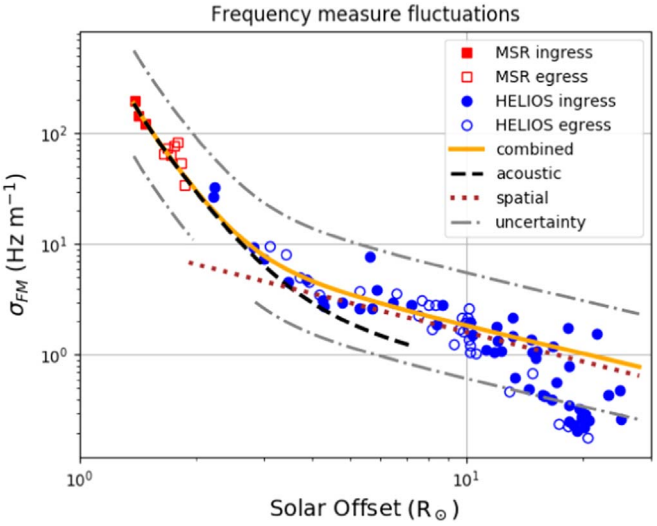

Figure 9. The composite *MESSENGER–HELIOS* frequency measure observations, shown with results of the FF model of combined component variances (Equation (30)). Acoustic wave contributions with $\epsilon_{\rm BL} = 0.017$ are shown with a dashed line, while the convected spatial density variations with $L_{\rm RAD} = 12{,}000$ km are shown with a dotted line. Uncertainty limits for the model are indicated with the dotted–dashed lines.

across the sounding LOS, to the native scaling frequency ν_c:

$$\epsilon_{\rm model} \equiv \epsilon_{\rm BL} \frac{\nu_{\rm shift}}{\nu_c}. \tag{26}$$

Since $\epsilon_{\rm BL}$ and ν_c are known, the problem reduces to specifying $\nu_{\rm shift}$ for acoustic waves and spatial density variations advected with the solar wind, as a function of solar offset.

Acoustic waves introduced at the lower corona are expected to damp out quickly, but turbulent actions in the corona could be expected to produce density waves locally. Our modeled density wave component is therefore considered to be a spectrum of locally generated slow waves exhibiting a baseline level of density fluctuation throughout the coronal region under study. Furthermore, we consider that the slow waves may travel in either direction at the speed of sound, C_s. With advection outward at solar wind speed $V_{\rm SW}$, we will have a combination of speeds $V_{\rm SW} + C_s$ and $V_{\rm SW} - C_s$ at the sounding LOS. When combined equally in quadrature, the rms speed is $V_{\rm acous} = \sqrt{V_{\rm SW}^2 + C_s^2}$. The characteristic source frequency of the acoustic wave is $f_{\rm wave}$ and the length scale for the acoustic waves is $L_{\rm acous} = C_s/f_{\rm wave}$. In the context of Equation (14), $f_{\rm wave} = \nu_c$ is specific to the given observational frequency band. The shifted acoustic wave frequency, $\nu_{\rm shift,acous} = V_{\rm acous}/L_{\rm acous}$, is

$$\nu_{\rm shift,acous} = \nu_c \frac{\sqrt{V_{\rm SW}^2 + C_s^2}}{C_s}. \tag{27}$$

As SO increases, the effect of solar wind speed cannot be ignored. For the acoustic waves, Equation (14) may be adapted to

$$\sigma^2_{\rm FM_{acous}} = r_e^2 \nu_c^2 \epsilon^2_{\rm BL} \frac{V_{\rm SW}^2 + C_s^2}{C_s^2} n_e^2 L_{\rm LOS} R \tag{28}$$

and the scaling for ϵ is then

$$\epsilon_{\rm model,acous} = \epsilon_{\rm BL} \frac{\sqrt{V_{\rm SW}^2 + C_s^2}}{C_s^2}. \tag{29}$$

At low SO, where $V_{\rm SW} \ll C_s$, $\nu_{\rm shift} \approx \nu_c$, Equations (28) and (29) simplify, and the results for baseline fluctuations are demonstrated. The results for Equation (28) are shown with a dashed line in Figure 9. The acoustic waves cannot explain the $\sigma_{\rm FM}$ findings beyond about $3.0R_\odot$. One change to the model to keep the density waves pertinent at higher SO could be to increase $\epsilon_{\rm BL}$, which is the underlying amplitude of density wave fluctuations. This was the approach taken by Miyamoto et al. (2014). The alternative is to introduce quasi-static spatial density variations that produce FFs on the sounding LOS as the variations are advected by the solar wind bulk flow. There is considerable intuitive appeal to bringing in this latter approach. In a general sense, the moving quasi-static density variations may roughly correspond to the "Sheeley blobs" (Sheeley et al. 1997) and more recent optical demonstrations of outflowing intensity enhancements (DeForest et al. 2018). In addition, the density variations will tend to be streamed radially, potentially introducing an element of SO-dependent anisotropy (roughly defined $L_{\rm RAD}/L_{\rm LOS} > 1$) in the correlation-scaled slabs. An exploration of anisotropic features will help to compare our model with work based on isotropic symmetric corona models (see the next section).

Quasi-static spatially distributed plasma density inhomogeneities advected past the sounding LOS result in FF. Let $L_{\rm RAD}$ be the characteristic radial length scale of the density inhomogeneities. Assuming the radial (∼horizontal) orientation of the system, the frequency of the density fluctuations $\nu_{\rm shift}$ on the observing LOS is found from the time derivative

$$\frac{d}{dt} = V_{\rm rad} \cdot \nabla. \tag{30}$$

The solar wind speed $V_{\rm SW}$ is assigned as $V_{\rm rad}$ and $\nabla \sim 1/L_{\rm RAD}$.

In analogy to the formulation for acoustic waves (Equation (28)), the advected spatial variations contribute to the observed frequency measure fluctuation as

$$\sigma^2_{\rm FM_{spatial}} = r_e^2 \nu_c^2 \epsilon^2_{\rm BL} \left[\frac{V_{\rm SW}}{L_{\rm RAD}} \frac{1}{\nu_c}\right]^2 n_e^2 L_{\rm LOS} R \tag{31}$$

and the scaling for ϵ is

$$\epsilon_{\rm model,spatial} = \epsilon_{\rm BL} \frac{V_{\rm SW}}{L_{\rm RAD}} \frac{1}{\nu_c} \tag{32}$$

in accordance with Equation (26).

The model is completed by combining the component variances

$$\sigma^2_{\rm FM_{MODEL}} = r_e^2 \nu_c^2 \epsilon^2_{\rm model} n_e^2 L_{\rm LOS} R \tag{33}$$

where $\epsilon_{\rm model}$ is

$$\epsilon_{\rm model} = \epsilon_{\rm BL} \sqrt{\frac{V_{\rm SW}^2 + C_s^2}{C_s^2} + \left[\frac{V_{\rm SW}}{L_{\rm RAD}\nu_c}\right]^2}. \tag{34}$$

We assign a value to $L_{\rm RAD}$ from observational results at $r = 10R_\odot$ using Equations (33) and (34). Using the

mean observed $\sigma_{FM} = 1.80$ Hz m^{-1}, $V_{SW} = 160$ km s^{-1}, $C_s = 85$ km s^{-1} we find $L_{RAD} = 12{,}000$ km for $\epsilon_{BL} = 0.017$ and $\nu_c = 0.0036$ Hz (based on $\alpha = 0.5$, Equation (15)). We hold L_{RAD} constant for the SO range under study.

Note that our approach uses a two point calibration: ϵ_{BL} is set from the low SO observations where acoustic waves dominate the observed fluctuations, whereas L_{RAD} is set at higher SO where the advected quasi-static density variations dominate the results. The calibration is specific to the frequency integration range and α used to obtain ν_c and to the SW speed model used to determine L_{RAD}.

Results of the two-component variances model are shown in Figure 9. The acoustic waves account for most of the observed frequency measure fluctuations up to about $3R_\odot$. The crossover between acoustic and spatial density variation dominance is apparent above $3R_\odot$, and the components are distinctly separated by the estimated sonic point of $6R_\odot$.

For an estimate of uncertainty, we combined in quadrature the fractional component uncertainties in n_e, L_{LOS} and ϵ. Since our n_e model was specifically constructed from results reported for epoch-relevant *MESSENGER* and *HELIOS* observations, we estimate the uncertainty in n_e to be no more than a factor of three. Uncertainty in L_{LOS} is based on magnetic field strength uncertainty, which is also guessed to be within a factor of three, but taken by its usage as the square root. Uncertainty in ϵ was taken to be 30%, as above. The combined uncertainty in σ_{FM} is a factor of 3.7.

The results of ϵ_{model} (Equation (34)) are plotted as lines over the observationally determined individual values for ϵ in Figure 8(a), using representative α assignments of 0.3, 0.5 and 0.67. The error limits for the $\alpha = 0.5$ model in Figure 8(a) (dotted lines), assuming the n_e model to be accurate, are derived from the combined uncertainties in ϵ_{BL} (10%), ν_c (30%) and estimated SW speed (25%).

The *MESSENGER* and *HELIOS* composite data form a continuous curve, despite the 34 year separation in observations that were taken by different teams on different instruments. The combined variances model fits the observations fairly well up to about $12R_\odot$. The scatter becomes greater above SO $12R_\odot$, where a distinct diminution of σ_{FM} beyond the uncertainty limits is apparent. This indicates a breakdown in the assumptions used in the model, with structural and dynamic changes in the corona. These changes might readily affect the power spectral index, electron density power law and turbulence spatial scales. Electron number density can vary up to an order of magnitude between the coronal holes and streamers (Pätzold et al. 1997), so we we raise the possibility that the outlier *HELIOS* measurements beyond $12R_\odot$ were obtained while the sounding LOS was outside a dense streamer region. Clarification of this matter will require analysis of other data sets.

The close match between the model and observations at low SO are particularly revealing because we expect complex, predominantly closed-field magnetic geometry in the equatorial regions out to at least the magnetic field "source surface" at about $2.5R_\odot$. In this regime, we would expect little effect from advected quasi-static density variations because the solar wind is poorly developed and flux tube orientations probably deviate from the radial flow scheme. However, the acoustic density waves could still contribute to FF fluctuations on the LOS, even with non-radial orientations. Until $r = 3R_\odot$, σ_{FM} trends with the acoustic wave component, as shown in Figure 9. These findings are consistent with the presence of compressive waves in the lower corona that contribute to observed frequency measure fluctuations, even when bulk plasma flow is slow and wave vectors are non-radial.

Our two-component model (Equations (33) and (34)) reproduces the observations fairly well up to $r = 12R_\odot$ without introducing any arbitrary changes to the parameters to obtain a fit. Our model operates using three fixed parameters, ϵ_{BL}, L_{RAD} and ν_c . The first two are found by calibration to the data at SO 1.4–1.7$R_\odot$ and $10R_\odot$ respectively, and the last is fixed by the frequency integration limits and the spectral index of the FM power spectrum. Aside from the constant r_e, the remaining variables are dependent on solar offset r: $n_e(r)$, $V_{SW}(r)$, $C_s(r)$, $L_{LOS}(r)$ and $R = rR_\odot$. If we were to fit the findings with advected acoustic waves only, as in the work by Miyamoto et al. (2014), then ϵ_{BL} would be forced to increase with increasing SO—the mechanism remains speculative (Suzuki & Inutsuka 2005). While we cannot be certain that the observed FF are not due entirely to advected acoustic waves or entirely to advection of the quasi-stationary disturbances, it is promising that no parameters had to be adjusted arbitrarily using the two-component model.

Generally speaking, FF due solely to advected spatial density variations would be expected to produce little FF in the low SO region because V_{sw} is small. We could compensate by lowering L_{RAD} at low SO. However, it would be odd to shrink the spatial length scales at low SO—if anything, we should find length scales shortening as the turbulent cascade evolves with increasing increasing SO. However, it is reasonable to consider that L_{RAD} as a fixed or slowly changing variable may apply only over a limited SO range. These adjustments to our model will require further data in future work.

There is also observational evidence to argue against use of advected spatial density variations exclusively in the model. We found no consistent differences between ingress and egress observations. If C_s was small or absent and spacecraft projected motion was a significant fraction of V_{SW}, then we would expect σ_{FM} to be larger in ingress than in egress due to a differential in speed of density disturbances moving across the LOS. This differential effect would be most noticeable at low solar offset, where V_{SW} is comparable to the *MESSENGER* LOS speed V_{MSR} of about 13 km s^{-1}. In this regime, the effective speed of fluctuations across the sounding LOS during ingress would be increased by V_{MSR}, whereas in egress it would be decreased by this amount. Our model explains this lack of observed difference between egress and ingress results by inclusion of compressive waves moving at the speed of sound, which is well above V_{MSR} and makes the difference negligible.

5. Isotropic Quasi-static Turbulence Model

We now give consideration to an alternative, well-studied model that is based on the bulk outflow of "frozen-in" turbulence across the sounding LOS. A number of early studies on radio scattering laid the groundwork for this model (e.g., Hollweg & Harrington 1968; Jokipii 1973; Woo 1978). Armand et al. (1987, 2003) and Efimov et al. (2008, 2010) presented an isotropic turbulence model to evaluate coronal FF. Their model assumes a quasi-static isotropic 3D spatial electron density inhomogeneity spectrum. This spatial density inhomogeneity pattern moves with the solar wind across the sounding LOS to produce the observed FF, without contribution from propagating density waves. Spectral index α characterizes the

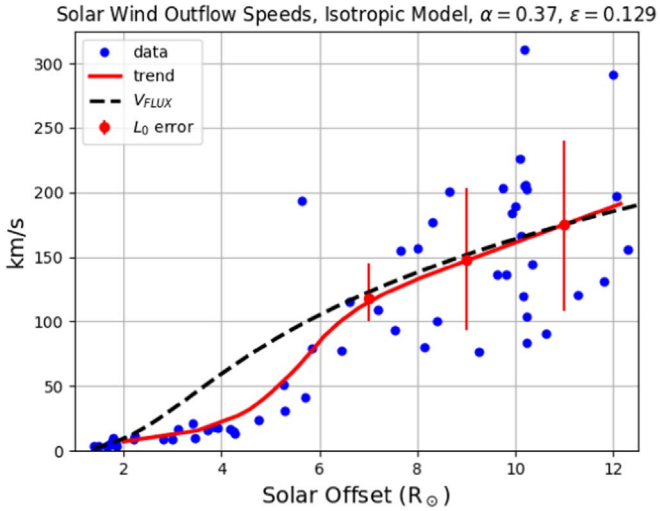

Figure 10. Solar wind velocity results using the isotropic turbulence equation (solid line—trend; dots—individual data points). For comparison, the $V_{\rm flux}$ (mass continuity) curve is shown as a dashed line. The illustrated error limits were based only on the uncertainty in the outer scale of turbulence.

frequency-dependence of the turbulence spectrum and appears prominently the final formula. In wavelength-normalized format, the Efimov–Armand isotropic turbulence model is:

$$\sigma_{\rm FM}^2 = r_e^2 \left\{ \frac{\alpha}{\pi(1-\alpha)} (\nu_{\rm up}^{1-\alpha} - \nu_{\rm low}^{1-\alpha}) \right\} \epsilon_{ru}^2 n_e{}^2 L_e V_{\rm SW}^{\alpha+1} L_0^{-\alpha} \tag{35}$$

where $\nu_{\rm up}$ and $\nu_{\rm low}$ are the upper and lower integration limits used in the power-law portion of the FF power spectrum, L_0 is the outer scale of turbulence (Bird et al. 2002), ϵ_{ru} is the fractional density fluctuation as determined in this particular paradigm and the other parameters are the same as described earlier. One may solve Equation (35) for $V_{\rm SW}$ by applying the $\sigma_{\rm FM}$ observations and the parameter estimates that are used above. It is necessary to assign a value to the estimated fractional fluctuation parameter, ϵ_{ru}. We note that the bracketed portion of (35) serves as the scaling factor on ϵ_{ru} based on the frequency integration limits and spectral index α. We roughly equate our baseline fractional fluctuation parameter $\epsilon_{\rm BL}$ to ϵ_{ru} using the bracketed scaling factor. For the practical integration limits $\nu_{\rm up} = 0.028$ Hz and $\nu_{\rm low} = 0.001$ Hz, and $\alpha = 0.37$ (see below), $\epsilon_{ru} = 0.129$. The relatively large ϵ_{ru} value is related to the theoretical development from the outer scale of turbulence, which is associated with a low wave number and widened frequency limits in the definite integral for determination of variance. In contrast, our formulation of $\epsilon_{\rm BL}$ was already defined by more restricted frequency limits of integration, and therefore presented a smaller fractional fluctuation value.

For the outer scale of turbulence, we used

$$L_0(r) = A_0 r^{\mu} \tag{36}$$

with $A_0 = 0.23 \pm 0.11\, R_\odot$ and $\mu = 0.82 \pm 0.13$ as given by Bird et al. (2002). The outer scale of turbulence has significant uncertainty, and is particularly poorly documented for low solar offset.

Spectral index α measurements are known to exhibit high variability, but is generally agreed to be less than the Kolmogorov value of 2/3 in the inner coronal regions and gradually increases to the Kolmogorov value by heliocentric distance $\approx 15\, R_\odot$ (Efimov et al. 2010; Yakovlev 2017). For illustration, we used $\alpha = 0.37$, a reasonable intermediate value between our *MESSENGER* finding of 0.55–0.58 and the values around 0.2 that are shown in Yakovlev (2017). The number density model was kept the same as used earlier (Equation (21)), and we again used $L_e \approx R$.

Figure 10 shows solar wind speed derived from the isotropic turbulence model (Equation (35)), compared to the speed curve $V_{\rm flux}$ from Equation (25). Above $7\, R_\odot$, the scatter is high but the trend does follow the speeds predicted by mass flux conservation. The considerable scatter reflects the dispersion in the $\sigma_{\rm FM}$ results seen in Figure 5. Up until about $5R_\odot$, the spread in the data is small and the corresponding outflow speeds are tightly grouped. Over $2–7R_\odot$, the isotropic turbulence model underestimates solar wind speed when compared to the expected mass flux speeds. Larger wind speeds at low solar offset would have required smaller ϵ_{ru} or increased L_0. Similar estimates for solar wind outflow speed below $7R_\odot$ can be found in other radio sounding studies, such as the work by Imamura et al. (2014). Their model for evaluation of intensity scintillations was also founded on the bulk flow of a quasi-static isotropic three-dimensional spatial turbulence spectrum, with the Kolmogorov spectral index assigned.

The lack of anisotropy in the classic models may help to explain the low wind speed estimates at low solar offset. Our model intrinsically introduced the possibility of anisotropy in the sense of setting the characteristic radial length scale $L_{\rm RAD}$ to the spatial density length along the horizontal slab, while separately setting the vertical integration length $L_{\rm LOS}$ to the expected local field line oscillation correlation length. We consider anisotropy as $L_{\rm RAD}/L_{\rm LOS}$ greater than one. The observed $\sigma_{\rm FM}^2$ resulted from the sum of element column density variances, $\sigma_{n_e}^2 L_{\rm LOS}^2$, along the LOS integration path. Over the effective LOS integration path, $L_e \approx R$, there are $R/L_{\rm LOS}$ such element variances, so the total LOS column density variance is $\sigma_{n_e}^2 L_{\rm LOS} R$, as contained in Equation (14). By the same reasoning, the isotropic case roughly replaces $L_{\rm LOS}$ with $L_{\rm iso}$, the length scale for isotropic spatial turbulence set for the specific observational frequency limits. Then, the column density fluctuation variance is $\sigma_{n_e}^2 L_{\rm iso} R$. Since $L_{\rm iso}$ is greater than $L_{\rm LOS}$ at low SO, the isotropic model produces a larger column density fluctuation and forces a lower calculated $V_{\rm SW}$ for a given $\sigma_{\rm FM}^2$ than does the stacked slab model, until $L_{\rm LOS} = L_{\rm iso}$. This lowering of the calculated velocity with the isotropic model is seen in Figure 10 below $\sim 7R_\odot$.

Although $L_{\rm RAD} = 12{,}000$ km at the scaling frequency $\nu_c = 3.6$ mHz, most of the spectral power resides in the low frequencies; e.g., 1–2 mHz, with corresponding length scales 19–38 Mm. The axial ratios associated with a radial length scale of say, 30 Mm, fall from 5 at $r = 2R_\odot$ to about 1 at $r = 12R_\odot$. Armstrong et al. (1990) demonstrated field-aligned density fluctuations with similar increases of axial ratio at low SO. Anisotropy was also demonstrated in coronal magnetic fluctuations inferred from Faraday rotation observations (Andreev et al. 1997). In our model, shorter length scale components reach equivalence to the correlation scale $L_{\rm LOS}$ at lower solar offsets than do the larger scale components. The anisotropy therefore fades to isotropy over a range of solar offsets for the range of length scales under study. If we take $r = 7R_\odot$ as the transition to mostly isotropic behavior in the

stacked slab representation, then it is then of considerable interest that the Efimov–Armand isotropic turbulence model produces solar wind speeds similar to our mass conservation speeds starting at $r = 7R_\odot$, at least out to 12 $R_\odot$.

In the study of coronal slow compressive waves by Miyamoto et al. (2014), the transverse integration length was equated to radial wavelength, essentially forcing a sort of 2D isotropic behavior into the results at all solar offsets. Since the isotropic condition may result in low wind speed estimates and/or low fractional density fluctuation ϵ determination, the low values $\epsilon < 0.01$ at close solar range found by Miyamoto et al. (2014) are not surprising. However, the physical interpretation of these diminished fractional density fluctuation estimates is unclear. Our fractional fluctuation baseline of 0.017 is somewhat low compared to Hollweg's value (Hollweg et al. 2010) of ~0.023–0.031, probably due to our lack of the higher amplitude, sub-mHz components that were missed by our 1 mHz low frequency integration cut-off.

An additional difference between our study and that of Miyamoto et al. (2014) is that they only evaluated selected segments that show the quasiperiodic component properties, presumably attributed to strong singular density waves, while we considered the observed fluctuations as a statistical ensemble result of uncorrelated density variations in stacked correlation-based slabs. Our model does not preclude the possibility of QPC results. A QPC may arise either from occasional random chance phase-alignments across flux tubes, or more significantly, as the result of a large density-generating event that introduces phase-aligned disturbances into a number of slabs simultaneously.

Beyond about $r = 12R_\odot$, the scatter in the pooled *HELIOS* observations becomes large, most likely due to the combined effects of less reliable Doppler noise estimates at small amplitude, and structural differences in the corona between the 1975 and 1976 observing campaigns. Although we cannot reliably extend the inferred velocity analysis out beyond $12R_\odot$ with these data, we look forward future studies utilizing contemporary, high-resolution FF data.

6. Conclusions

We presented a simplified model for coronal electron density fluctuations in a system of stacked density fluctuation slabs to analyze radio FFs obtained from spacecraft transcoronal sounding near equatorial solar minimum. The observations included *MESSENGER* 2009 occultation data probing the corona down to $1.38R_\odot$ and archival *HELIOS* Doppler noise measurements out to $25R_\odot$. The power spectrum of FF originates from a corresponding power spectrum of density fluctuations, from which σ_{n_e} is obtained computationally. The fractional density fluctuation parameter, ϵ, was found to exhibit a baseline of about 1.7% at low solar offset for the specific fluctuation frequency band that we studied (1–28 mHz). The fractional density fluctuation, as calculated from observed $\sigma_{\rm FM}$, increased above the baseline up to about 7.5% by $r = 10R_\odot$, with a curve not unlike that of the modeled solar wind outflow speed. We constructed a two-component model to predict FF variance and the fractional density fluctuation ϵ based on propagating density waves and spatial density variations, both advected with the solar wind. Our model predicted observations fairly well up to about $12R_\odot$, suggesting that the randomized acoustic or slow magnetoacoustic waves explain much of the FF variance at low solar offset, while convected spatial variation density variations dominate the observations as the solar wind accelerates. The model was successful at low SO, despite more complex, non-radial magnetic structuring in closed-field sub-streamer regions. Distinct anisotropy in density inhomogeneity length scales was inherent to the model at low SO, but by about $7R_\odot$ most of the component spatial lengths were below slab width $L_{\rm LOS}$, which allowed a rough approximation to isotropic behavior. Interestingly, at and above $7R_\odot$, the 3D isotropic quasi-static turbulence model (Efimov et al. 2008) reproduced solar wind outflow speeds expected from the literature and mass flux considerations, at least to $12R_\odot$.

The highlights of the present approach follow: 1. The method brings stacked correlation-scale slab structuring of the corona into the density inhomogeneity analysis. 2. The model produces anisotropic density structuring at low solar offset due to magnetic field strength control of slab integration length ($L_{\rm LOS}$). 3. The model invokes wave propagation close to the Sun to explain the lack of consistent difference between egress and ingress FF observations at low solar offset. 4. The model assumes mass conservation along the slab elements, and sets predicted solar wind speed based on $V_{\rm SW} = 250\ {\rm km\ s^{-1}}$ at SO $r = 20R_\odot$. 5. The modeled sonic point is $6R_\odot$. 6. The close correspondence between the observations and our model predictions suggests the presence of ubiquitous plasma density fluctuations of temporal and spatial character in the corona. These density fluctuations, even at a relatively low fractional amplitude, seem to produce the observed FF. Whether the slow compressive waves play a direct role in coronal energy dissipation or perhaps represent a marker for energy transfer from Alfvén waves needs additional study. A correlative study between co-measured Faraday rotation fluctuations and FFs could be particularly useful in distinguishing compressive MHD waves from acoustic waves. 7. Our mass flux derived speeds are generally consistent with results from the optical difference-images study by Sheeley et al. (1997). 8. The two-component model for FM fluctuations reproduced the observations out to at least $12R_\odot$. However, this is still a preliminary model. More optical and radio sounding data, ideally concurrent observations, are desirable to follow up on these impressions, refine the model and clarify the expected FF at higher SO. Lastly, the long-awaited Parker Solar Probe (Bale et al. 2016; Kasper et al. 2016) mission should be uniquely poised to offer contemporary coronal radio sounding opportunities, with concurrent in situ measurements, with which to refine our understanding of the solar wind and validate space radio physics models.

We thank Paul Song, Igor Chashey, and Divya Oberoi for helpful discussions. Michael Bird provided technical expertise on the *HELIOS* data. We also thank Ariel Wexler for computing consultation. Special appreciation to Peter Macneice and the Community Coordinated Modeling Center team for securing the solar magnetograms and processing the global coronal magnetic field models displayed in Figure 1. We appreciate the reviewer's comments, which greatly improved the final report. D.W. thanks Stephen Marsden for ongoing administrative supervision. The University of Southern Queensland research office kindly supported publication of this work.

ORCID iDs

David B. Wexler https://orcid.org/0000-0002-5763-6267
Elizabeth A. Jensen https://orcid.org/0000-0003-0216-6621

References

Andreev, V. E., Efimov, A. I., Samoznaev, L. N., Chashei, I. V., & Bird, M. K. 1997, SoPh, 176, 387
Andreev, V. E. M., Bird, K., et al. 1997, AstL, 23, 194
Armand, N. A., Efimov, A. I., Samoznaev, L. N., et al. 2003, Journal of Communications Technology and Electronics, 48, 970
Armand, N. A., Efimov, A. I., & Yakovlev, O. I. 1987, A&A, 183, 135
Armstrong, J. W., Coles, W. A., Kojima, M., & Rickett, B. J. 1990, ApJ, 358, 685
Bale, S. D., Goetz, K., Harvey, P. R., et al. 2016, SSRv, 204, 49
Berman, A. L., & Rockwell, S. T. 1975, DSNPR, 42, 231
Berman, A. L., Wackley, J. A., & Rockwell, S. T. 1976, DSNPR, 42, 121
Bird, M. K., & Edenhofer, P. 1990, in Physics of the Inner Heliosphere I, ed. R. Scheween & E. Marsch (Berlin: Springer-Verlag), 13
Bird, M. K., Efimov, A. I., Andreev, V. E., et al. 2002, AdSpR, 30, 447
Chashei, I. V., Efimov, A. I., Samoznaev, L. N., Plettemeier, D., & Bird, M. K. 2005, AdSpR, 36, 1454
Cranmer, S. R. 2010, ApJ, 710, 676
Cranmer, S. R., Asgari-Targhi, M., Miralles, M. P., et al. 2015, RSPTA, 373, 20140148
Cranmer, S. R., van Ballegooijen, A. A., & Edgar, R. J. 2007, ApJS, 171, 520
DeForest, C. E., Howard, R. A., Velli, M., Viall, N., & Vourlidas, A. 2018, ApJ, 862, 1
De Pontieu, B., McIntosh, S. W., Carlsson, M., et al. 2007, Sci, 318, 1574
Edenhofer, P., Lueneburg, E., Esposito, P. B., et al. 1977, JGZG, 42, 673
Efimov, A. I., Bird, M. K., Chashei, I. V., & Samoznaev, L. N. 2004, AdSpR, 33, 701
Efimov, A. I., Lukanina, L. A., Rogashkova, A. I., et al. 2015a, ARep, 59, 313
Efimov, A. I., Lukanina, L. A., Rogashkova, A. I., et al. 2015b, SoPh, 290, 2397
Efimov, A. I., Lukanina, L. A., Samoznaev, L. N., et al. 2010, ARep, 54, 446
Efimov, A. I., Lukanina, L. A., Samoznaev, L. N., et al. 2012, AdSpR, 49, 500
Efimov, A. I., Lukanina, L. A., Samoznaev, L. N., Chashei, I. V., & Bird, M. K. 2010, Journal of Communications Technology and Electronics, 55, 1253
Efimov, A. I., Samoznaev, L. N., Bird, M. K., Chashei, I. V., & Plettemeier, D. 2008, AdSpR, 42, 117
Efimov, A. I., Samoznaev, L. N., Rudash, V. K., et al. 2007, ARep, 51, 687
Efimov, A. I., Yakovlev, O. I., Rudash, V. K., Chashei, I. V., & Shishov, V. I. 1993, ARep, 37, 542
Hollweg, J. V. 1978, GeoRL, 5, 731
Hollweg, J. V., Bird, M. K., Volland, H., et al. 1982, JGR, 87, 1
Hollweg, J. V., Cranmer, S. R., & Chandran, B. D. G. 2010, ApJ, 722, 1495
Hollweg, J. V., & Harrington, J. V. 1968, JGR, 73, 7221
Imamura, T., Tokumaru, M., Isobe, H., et al. 2014, ApJ, 788, 117
Jensen, E. A., Frazin, R., Heiles, C., et al. 2016, SoPh, 291, 465
Jensen, E. A., Nolan, M., Bisi, M. M., Chashei, I., & Vilas, F. 2013, SoPh, 285, 71
Jokipii, J. R. 1973, ARA&A, 11, 1
Kasper, J. C., Abiad, R., Austin, G., et al. 2016, SSRv, 204, 131
Klimchuk, J. A. 2015, RSPTA, 373, 20140256
McIntosh, S. W., de Pontieu, B., Carlsson, M., et al. 2011, Natur, 475, 477
Mercier, C., & Chambe, G. 2015, A&A, 583, A101
Miyamoto, M., Imamura, T., Tokumaru, M., et al. 2014, ApJ, 797, 51
Muhleman, D. O., & Anderson, J. D. 1981, ApJ, 247, 1093
Nakariakov, V. M., & Verwichte, E. 2005, LRSP, 2, 3
Newkirk, G., Jr. 1967, ARA&A, 5, 213
Patzold, M., Bird, M. K., Volland, H., et al. 1987, SoPh, 109, 91
Pätzold, M., Hahn, M., Tellmann, S., et al. 2012, SoPh, 279, 127
Pätzold, M., Tsurutani, B. T., & Bird, M. K. 1997, JGR, 102, 24151
Sakurai, T. 2017, PJAB, 93, 87
Sheeley, N. R., Wang, Y.-M., Hawley, S. H., et al. 1997, ApJ, 484, 472
Song, P., & Russell, C. T. 1999, SSRv, 87, 387
Spruit, H. C. 1981, NASSP, 450, 385
Suzuki, T. K., & Inutsuka, S.-i. 2005, ApJL, 632, L49
Tomczyk, S., McIntosh, S. W., Keil, S. L., et al. 2007, Sci, 317, 1192
Vierinen, J., Norberg, J., Lehtinen, M. S., et al. 2014, RaSc, 49, 1141
Wexler, D. B., Jensen, E. A., Hollweg, J. V., et al. 2017, SpWea, 15, 310
Woo, R. 1978, ApJ, 219, 727
Yakovlev, O. I. 2017, R&QE, 60, 259
Yakovlev, O. I., & Pisanko, Y. V. 2018, AdSpR, 61, 552